

# Skeleton-to-Image Encoding: Enabling Skeleton Representation Learning via Vision-Pretrained Models

Siyuan Yang, Jun Liu, Hao Cheng, Chong Wang, Shijian Lu, Hedvig Kjellstrom, Weisi Lin, *Fellow, IEEE* and Alex C. Kot, *Life Fellow, IEEE*



**Abstract**—Recent advances in large-scale pretrained vision models have demonstrated impressive capabilities across a wide range of downstream tasks, including cross-modal and multi-modal scenarios. However, their direct application to 3D human skeleton data remains challenging due to fundamental differences in data format. Moreover, the scarcity of large-scale skeleton datasets and the need to incorporate skeleton data into multi-modal action recognition without introducing additional model branches present significant research opportunities. To address these challenges, we introduce Skeleton-to-Image Encoding (S2I), a novel representation that transforms skeleton sequences into image-like data by partitioning and arranging joints based on body-part semantics and resizing to standardized image dimensions. This encoding enables, for the first time, the use of powerful vision-pretrained models for self-supervised skeleton representation learning, effectively transferring rich visual-domain knowledge to skeleton analysis. While existing skeleton methods often design models

tailored to specific, homogeneous skeleton formats, they overlook the structural heterogeneity that naturally arises from diverse data sources. In contrast, our S2I representation offers a unified image-like format that naturally accommodates heterogeneous skeleton data. Extensive experiments on NTU-60, NTU-120, and PKU-MMD demonstrate the effectiveness and generalizability of our method for self-supervised skeleton representation learning, including under challenging cross-format evaluation settings.

**Index Terms**—Skeleton representation learning, skeleton-to-image encoding, vision-pretrained models.

## 1 INTRODUCTION

Recent years have witnessed the remarkable success of large-scale vision-pretrained models, such as Vision Transformers (ViTs) [1], Masked Autoencoders (MAE) [2], and Vision-Language Models (VLMs) [3], [4], across diverse visual recognition and understanding tasks. These models leverage abundant image data to learn transferable representations and are increasingly adapted to other modalities, including depth maps [5], [6], IR images [7], [8], video sequences [9]–[11], and even point clouds [12], [13]. A common strategy is to project non-image modalities into 2D formats, enabling direct use of image-pretrained models. While this works for dense 3D data like point clouds, applying similar

- Siyuan Yang and Hedvig Kjellstrom are with the KTH Royal Institute of Technology, Stockholm, Sweden. E-mail: {siyuany, hedvig}@kth.se
  - Hao Cheng is with the Hebei University of Technology, Tianjin, China. E-mail: chenghao@hebut.edu.cn
  - Chong Wang, Shijian Lu, and Weisi Lin are with the Nanyang Technological University, Singapore. E-mail: {wang1711, Shijian.Lu, wslin}@ntu.edu.sg
  - Jun Liu is with the Lancaster University, Lancaster, U.K. E-mail: j.liu81@lancaster.ac.uk
  - Alex C. Kot is with the Shenzhen MSU-BIT University, Shenzhen, China, and VinUniversity, Hanoi, Vietnam. E-mail: acokot@ntu.edu.sg
- Corresponding author: Jun Liu

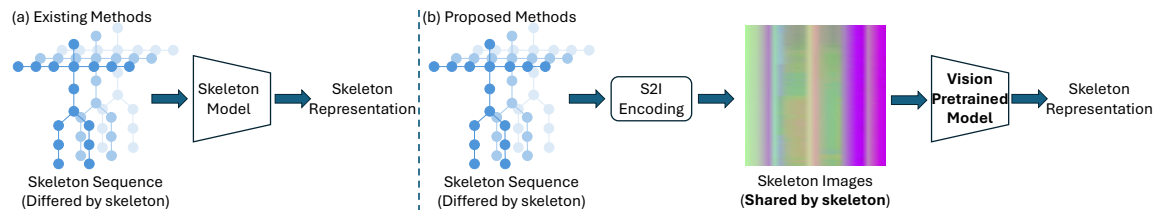


Fig. 1: The existing methods train the skeleton models directly, while the proposed method converts skeleton data into image-like data and then train with the pre-trained vision models.

projections to 3D skeleton data poses unique challenges. Skeletons are inherently sparse (only 15-30 joints per frame) and exhibit articulated structures with strong semantic relationships—unlike unstructured point clouds. Moreover, skeleton sequences span temporal dimensions critical for motion understanding, making naive 2D projections inadequate.

While directly applying vision models to skeleton data is non-trivial, skeleton-based representation learning remains fundamental for understanding human motion. Skeleton data provides a compact, appearance-invariant, and high-level abstraction of human activities, making it particularly valuable for tasks such as action recognition, gait analysis, and human-computer interaction. Furthermore, as multi-modal action recognition gains traction, skeleton data serves as a complementary modality that can enhance robustness and interpretability when integrated with dense visual modalities such as RGB and depth. However, the scarcity of large-scale annotated skeleton datasets and the incompatibility of skeleton structures with existing vision model architectures limit current methods’ generalization ability across diverse tasks and scenarios.

To overcome these challenges, we introduce an approach that leverages pretrained Vision Models—such as MAE [2] and DiffMAE [14]—for skeleton representation learning. This extends the use of vision models beyond 2D images to the 3D skeleton domain by transferring rich knowledge from large-scale image pretraining. At the core of this approach is our proposed **Skeleton-to-Image Encoding (S2I)**, a novel representation method that reformats skeleton sequences into image-like representation compatible with vision models. Specifically, the 3D joint coordinates

$(x, y, z)$  are directly mapped to RGB channels, converting motion patterns into pseudo-images. To ensure semantic consistency, we first partition skeleton joints into five body parts: torso, left arm, right arm, left leg, and right leg. These are then reordered by following the body part sequence, and within each part, joints are further sorted in a top-down manner based on their physical positions. We then stack these reordered joints across the temporal dimension, producing a spatial-temporal image-like representation of the entire skeleton sequence. Finally, the generated representation is resized to the standard image input size ( $224 \times 224$ ), enabling seamless integration with vision model inputs. As a result, our method enables, for the first time, the direct application of powerful pretrained vision models for self-supervised skeleton representation learning, effectively transferring rich visual domain knowledge to the skeleton domain without requiring task-specific architectural modifications. A visual comparison between existing skeleton pipelines and our approach is shown in Figure 1.

Current skeleton-based methods are typically designed for homogeneous skeleton formats, relying on fixed joint definitions and dataset-specific architectures. Such designs limit their scalability and make it difficult to accommodate skeleton data with varying joint configurations, coordinate systems, or capture devices. As a result, these methods struggle in cross-format scenarios, where skeleton layouts differ significantly across datasets. In contrast, our proposed S2I provides a unified and format-agnostic representation framework. By abstracting skeleton data into a consistent image-like structure, our method naturally supports joint training across multiple heterogeneous skeleton datasets. This capability

enables universal skeleton representation learning, where diverse skeleton formats can be leveraged together to enhance model generalization and capture richer motion dynamics.

Through extensive experiments on benchmark datasets, including NTU-60, NTU-120, and PKU-MMD, we demonstrate that our method achieves competitive performance in self-supervised skeleton representation learning. Notably, our approach shows exceptional effectiveness in challenging cross-format evaluation, exhibiting strong generalizability across heterogeneous skeleton formats.

Our contributions can be summarized as follows: (1) We propose a novel pipeline that leverages vision-pretrained models and their weights for skeleton-based representation learning, bridging the modality gap between images and skeleton sequences. (2) We introduce Skeleton-to-Image Encoding, a unified representation method that reformats sparse 3D skeleton data into image-like inputs, compatible with vision models and resilient to skeleton format variations. (3) We are the first to explore heterogeneous skeleton representation learning and propose a universal skeleton pretraining strategy, enabling cross-format learning across multiple skeleton datasets.

## 2 RELATED WORKS

### 2.1 Skeleton Action Recognition

In recent years, deep learning has been widely used in skeleton action recognition due to its strong capacity for feature extraction and representation learning. Existing methods typically adopt Recurrent Neural Networks (RNNs) [15]–[17], Convolutional Neural Networks (CNNs) [18]–[20], Graph Convolutional Networks (GCNs) [21]–[23], and Transformers-based models [24], [25] to directly learn skeleton representations. However, most prior methods are tailored to homogeneous skeleton formats, assuming fixed joint numbers. Such designs inherently limit their scalability and generalization to datasets with diverse skeleton structures. In contrast, our S2I representation offers a format-agnostic solution that naturally handles heterogeneous skeleton layouts, enabling more flexible and robust skeleton representation learning.

### 2.2 Self-Supervised Skeleton Representation Learning

Self-supervised skeleton representation learning has become a promising direction to reduce reliance on costly manual annotations. Recent methods mainly adopt contrastive learning [26]–[28] and masked modeling [29]–[31] to learn discriminative features from unlabeled skeleton data. In contrast, large-scale pretrained vision models have shown remarkable transferability across diverse downstream tasks and even different modalities. However, leveraging such pretrained models for skeleton data remains largely unexplored due to the inherent gap in data formats. In this work, we propose S2I, which reformats skeleton sequences into image-like representations, enabling the direct use of vision-pretrained models for skeleton tasks.

### 2.3 Self-Supervised Representation Learning

Self-supervised learning has gained significant traction in computer vision for its ability to learn effective representations without manual annotations. Contrastive learning methods exploit augmentation invariance to learn instance-discriminative features from images and videos [32]–[34]. More recently, masked modeling has emerged as a powerful alternative to contrastive methods. MAE [2] reconstructs masked pixel values using an asymmetric encoder-decoder design, providing a simple yet effective framework for visual representation learning. BEiT [35] follows a mask-then-predict strategy, using visual tokens generated by a pre-trained tokenizer as prediction targets. MaskFeat [36] instead predicts HOG features rather than raw pixels, providing a task-agnostic learning objective. DiffMAE [14] further enhances MAE by introducing a denoising diffusion process to iteratively reconstruct masked regions. In this work, we evaluate our proposed S2I representation using both MAE and DiffMAE pretrained models.

## 3 METHOD

### 3.1 Skeleton-to-Image Encoding

As discussed in Section 1, our objective is to leverage vision-pretrained models for skeleton

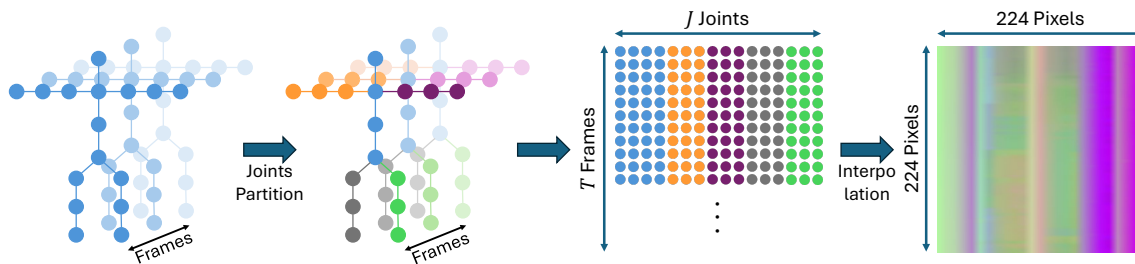


Fig. 2: Illustration of the Skeleton-to-Image Encoding (S2I) process, which transforms skeleton sequences into image-like representations via joint partitioning, temporal stacking, and interpolation.

representation learning. This enables the effective utilization of large-scale vision models and their pretrained weights for skeleton tasks. Furthermore, adopting a unified vision model facilitates multi-modal action recognition, where diverse data modalities can be seamlessly integrated.

To achieve this, skeleton data must be reformatted into a representation compatible with image-based models. Specifically, it is essential to encode spatial-temporal information from skeleton sequences in a form analogous to image data, thereby enabling knowledge transfer from pre-trained vision models. However, a fundamental challenge arises from the inherent differences in data structures. While image data is typically represented as tensors of size  $3 \times 224 \times 224$  for vision models, skeleton sequences are structured as  $T \times J \times 3$ , where  $T$  denotes the temporal length of the sequence, and  $J \times 3$  represents the 3D coordinates  $(x, y, z)$  of skeleton joints. To bridge this discrepancy, we propose a straightforward yet effective mapping strategy. The 3D joint coordinates  $(x, y, z)$  are directly assigned to the RGB channels of an image, with each spatial axis corresponding to one color channel. The remaining challenge is to project the  $T \times J$  spatial-temporal data into the  $224 \times 224$  image, ensuring compatibility with standard vision model inputs.

To bridge the gap between skeleton sequences and image-based model inputs, we propose **Skeleton-to-Image Encoding (S2I)**, a novel representation that transforms skeleton sequences into dense, image-like data compatible with vision models (e.g., MAE, DiffMAE), as illustrated in Figure 2. Specifically, we partition the human skeleton into five semantic body parts: spine, left

arm, right arm, left leg, and right leg. This strategy, widely adopted in prior works [37]–[39], follows the kinematic structure of the human body and can be generalized across skeleton formats.

Within each part, joints are arranged along their kinematic chain, ordered by distance from the torso. For example, joints in the left leg are sequenced as: left hip  $\rightarrow$  left knee  $\rightarrow$  left ankle  $\rightarrow$  left foot. This ordering preserves the spatial relationships inherent in the skeleton structure. For temporal modeling, the 3D positions of each joint across  $T$  frames are stacked to form a spatio-temporal feature map of size  $T \times J$ , where  $(x, y, z)$  coordinates are assigned to the RGB channels of the image. Finally, to match the input requirements of vision models (e.g.,  $224 \times 224$ ), we apply linear interpolation along both temporal and joint dimensions, resizing them independently to a fixed resolution of  $224 \times 224$ . This yields an image-like representation of the skeleton sequence while preserving essential spatial-temporal patterns.

### 3.2 Vision Representation Models

Our proposed S2I reformats skeleton data into image-like data, enabling seamless application of vision-pretrained models for skeleton representation learning. Unlike skeleton networks, our approach leverages the general architecture and pretrained weights of powerful vision models.

In this work, we evaluate two representative vision models to demonstrate the effectiveness of our representation: MAE [2] and DiffMAE [14]. Both models are originally designed for image representation learning and pretrained on large-scale ImageNet, providing rich visual priors that

can be effectively transferred to the skeleton domain through our unified representation. **MAE** learns visual representations by reconstructing masked image patches from the visible context. Leveraging our S2I encoding to convert skeleton sequences into image-like data, we initialize MAE with ImageNet-pretrained weights and perform skeleton pretraining via masked reconstruction. **DiffMAE** further enhances this framework by incorporating iterative denoising processes inspired by diffusion models. Using the same S2I inputs, we similarly initialize DiffMAE from ImageNet-pretrained weights and conduct skeleton pretraining through diffusion-based reconstruction.

The skeleton-pretrained models are evaluated on downstream skeleton tasks to validate the effectiveness of our proposed S2I representation. While we focus on MAE and DiffMAE in this work, our S2I representation is compatible with a broad range of vision models, including emerging generative and multimodal architectures.

**Application & Advantage.** Our S2I reformats skeleton sequences into image-like representations that are inherently robust to variations in skeleton structures. By abstracting skeleton data into a unified format, it enables seamless representation of diverse skeleton layouts without relying on dataset-specific joint definitions. In contrast, conventional skeleton-based methods are tightly coupled to homogeneous skeleton formats, assuming fixed joint numbers, which limits their scalability and generalization across datasets with differing skeleton structures. Even recent work [40], [41] has attempted cross-format settings, but their evaluations still rely on shared joint subsets, thereby fundamentally adhering to homogeneous representations.

Our approach differs by introducing a format-agnostic representation paradigm. By decoupling skeleton representations from dataset-specific joint configurations, it enables seamless integration of skeleton data from heterogeneous sources. As a result, S2I naturally supports **cross-format representation learning**, allowing models trained on one skeleton format to generalize to others. It also enables **universal representation pre-training** by jointly leveraging diverse skeleton datasets, similar to practices in large-scale image

pretraining, without requiring task-specific architectural changes. A visual comparison between conventional skeleton pipelines and the two proposed settings is provided in the Appendix D.

### 3.3 Mask Sampling Strategy

The effectiveness of masked modeling largely depends on the masking strategy employed during pretraining. To optimize representation learning for skeleton data, we investigate several masking strategies applicable to both image-based and skeleton-specific contexts. **Random Masking** is the standard approach used in image-based masked modeling [2], where image patches are randomly masked without considering spatial relationships. Formally, given a mask ratio  $r$ , we randomly select  $\lfloor r \times N \rfloor$  patches to mask from the total  $N$  patches in the skeleton image representation. **Block Masking** increases pretraining task difficulty by masking contiguous regions of the input. Starting from randomly selected seed positions, blocks of adjacent patches are masked together, encouraging the model to learn stronger local structural relationships. Beyond these general strategies, we introduce two skeleton-specific masking schemes designed to better capture the unique spatial-temporal structure of human motion: **Joint Masking** focuses on the spatial domain by randomly masking joints across the skeleton body, challenging the model to infer missing joint positions based on articulated body structure. **Temporal Masking** targets the temporal dimension by masking entire frames or temporal slices, encouraging the model to capture dynamic motion patterns from partial sequences.

### 3.4 Training objectives

We adopt a two-stage training pipeline for skeleton action recognition, leveraging our Skeleton-to-Image (S2I) representation to adapt vision-pretrained models to the skeleton domain.

In the first stage, we perform *self-supervised skeleton representation learning* by applying masked modeling on our S2I representation, using the ImageNet-pretrained MAE [2] and DiffMAE [14] as backbones. Given a skeleton sequence  $\mathbf{X} \in \mathbb{R}^{3 \times 224 \times 224}$  transformed via S2I, we apply masked modeling to learn skeleton

representations: For MAE, we minimize the reconstruction loss between the original input and the reconstruction of the masked patches:

$$\mathcal{L}_{\text{MAE}} = \frac{1}{|\mathcal{M}|} \sum_{i \in \mathcal{M}} \left\| \hat{\mathbf{X}}_i - \mathbf{X}_i \right\|_2^2, \quad (1)$$

where  $\mathcal{M}$  denotes the set of masked patches,  $\hat{\mathbf{X}}_i$  is the reconstructed patch, and  $\mathbf{X}_i$  is the ground truth. For DiffMAE, we follow [14] and reconstruct the masked regions through a denoising diffusion process, conditioned on the visible parts. The loss is defined as:

$$\mathcal{L}_{\text{DiffMAE}} = \mathbb{E}_{t, x_0, \epsilon} \left\| x_m^0 - D_\theta(x_m^t, t, E_\phi(x_v^0)) \right\|_2^2, \quad (2)$$

where  $x_m^0$  is the original masked region,  $x_m^t$  is the noised version at diffusion step  $t$ ,  $x_v^0$  is the visible region,  $E_\phi$  denotes the encoder, and  $D_\theta$  is the diffusion decoder.

In the second stage, we evaluate the skeleton-pretrained encoders on downstream *skeleton action recognition* tasks by attaching a classification head and optimizing with cross-entropy loss:

$$\mathcal{L}_{\text{CE}} = - \sum_{c=1}^C y_c \log \hat{y}_c, \quad (3)$$

where  $C$  is the number of classes,  $y_c$  is the ground-truth label, and  $\hat{y}_c$  is the predicted probability. Depending on the evaluation protocol, we either perform linear probing with a frozen encoder or fine-tune the entire model.

## 4 EXPERIMENTS

### 4.1 Datasets

For evaluation, we conduct experiments on five datasets: NTU RGB+D 60 dataset (NTU-60) [42], NTU RGB+D 120 dataset (NTU-120) [43], PKU-MMD [44], Northwestern-UCLA (NW-UCLA) [45], and Toyota Smarthome (Toyota) [46]. The first three use 25-joint skeletons, while NW-UCLA and Toyota contain 20 and 13 joints.

**NTU-60** [42] is the most widely used benchmark for skeleton action recognition, comprising 56,880 skeleton sequences across 60 action classes performed by 40 subjects. Each sample contains at most two subjects, captured from three camera

views using Kinect v2. In our experiments, we follow the standard cross-subject (C-sub) and cross-view (C-view) evaluation protocols.

**NTU-120** [43] is the largest skeleton-based action recognition dataset to date, containing 114,480 samples across 120 action classes, collected from 106 subjects across 32 setups with varying locations and backgrounds. We follow the official cross-subject (C-sub) and cross-setup (C-set) evaluation protocols for benchmarking.

**PKU-MMD** [44] is a large-scale benchmark for 3D human action understanding, featuring approximately 20,000 action instances in 51 categories. PKU-MMD consists of two subsets: Part I (easier, cleaner data) and Part II (challenging, with significant skeleton noise from large view variations). We follow the cross-subject protocol for both subsets in our experiments.

**NW-UCLA** [45] contains 1,494 action samples from 10 classes, performed by 10 subjects and captured using three Kinect v1 cameras. Each skeleton consists of 20 joints. Following [45], we use samples from cameras V1 and V2 for training, and samples from camera V3 for testing.

**Toyota** [46] is a real-world dataset for daily living activity recognition, containing 16,115 videos across 31 classes. We conduct transfer learning experiments under both cross-subject (CS) and cross-view1 (CV1) settings.

### 4.2 Experimental Setup

**Network Architecture.** For both MAE and DiffMAE, we adopt the ViT-B architecture as the encoder. The decoder consists of eight transformer blocks, each with a channel dimension of 512. In DiffMAE, the decoder follows a cross-self attention design inspired by the original Transformer encoder-decoder structure. Specifically, in each decoder block, the noised tokens first attend to the visible latent representations via a cross-attention layer, followed by self-attention among noise tokens to refine predictions.<sup>1</sup>

**Data Processing Details.** For NTU-60, NTU RGB-120, PKU-MMD dataset, and Toyota, we follow

<sup>1</sup> Detailed network configurations and more implementation details are provided in Appendix A, Appendix B, and Appendix C.

the data pre-processing in [47], sequence level translation based on the first frame is performed to be invariant to the initial positions. If one frame contains two persons, we split the frame into two frames by making each frame contain one human skeleton. For the NW-UCLA dataset, we adopt the data pre-processing in [48].

**Implementation Details.** For the self-supervised skeleton learning stage, we initialize the models with ImageNet-pretrained MAE and DiffMAE checkpoints, and follow their default implementation configurations [2], [14].<sup>1</sup> For skeleton action recognition, we use SGD with Nesterov momentum (0.9) for linear probing, with an initial learning rate of 0.2 decayed via cosine annealing. For fine-tuning, we employ the AdamW optimizer with an initial learning rate of 0.001, decayed by cosine annealing. All skeleton action recognition experiments are trained for 100 epochs. The batch size is set to 128 for all datasets, except for NW-UCLA dataset, where a smaller batch size of 32 is used. Our method is implemented in PyTorch, and all experiments are conducted on NVIDIA RTX A6000 GPUs.

### 4.3 Ablation Study

We conduct ablation studies on the NTU-60 C-sub to evaluate three key aspects of our method: the effectiveness of Skeleton-to-Image representation, the impact of image-pretrained weights, and the choice of masking strategies.

**Effectiveness of Skeleton-to-Image Representation with Vision Models.** To evaluate the viability of using image-based models for skeleton representation learning, we evaluate MAE and DiffMAE architectures in combination with our proposed Skeleton-to-Image Encoding. As shown in Table 1, both models achieve strong performance after skeleton SSL pretraining, followed by linear probing or fine-tuning, demonstrating the viability of vision models for skeleton representation learning when equipped with appropriate representation strategies. These results demonstrate that, despite being designed for dense image data, vision models can effectively process structured skeleton sequences when equipped with appropriate representations. Skeleton-to-Image Encoding serves as an effective bridge, enabling the

reuse of powerful vision models without task-specific architectural modifications.

**Impact of Image-Pretrained Weights.** We examine the benefit of ImageNet-pretrained weights by comparing models trained from scratch and models initialized with pretrained weights. Table 1 shows that image-pretraining yields substantial gains in both linear probing and fine-tuning settings. In the linear probing scenario, pretrained MAE improves from 52.0% (scratch) to 72.2%, while pretrained DiffMAE improves from 52.0% to 71.3%. This substantial gap highlights the benefit of transferring generic visual representations to the skeleton domain. Furthermore, even after Skeleton Pretrain, pretraining with image data continues to provide notable gains, underscoring the importance of leveraging large-scale image-pretrained weights. These results demonstrate that image-pretrained weights offer rich and transferable visual knowledge, serving as a strong initialization for skeleton representation learning and significantly enhancing performance. Given DiffMAE’s consistently superior performance, we adopt it as the **default backbone** for subsequent studies and comparisons.

**Effect of Masking Ratio.** We investigate the influence of different masking ratios under the NTU-60 C-sub setting using DiffMAE. As shown in Figure 3, increasing the masking ratio generally improves representation quality, with 75% yielding the best results in both linear probing and fine-tuning. Notably, linear probing performance shows a larger gain (+8% improvement), while fine-tuning results are less sensitive (around 1% difference). Based on these findings, we adopt a 75% masking ratio as the default setting for subsequent ablation studies and main comparisons.

**Comparison of Masking Strategies.** We compare various masking strategies: joint, temporal, random, and group masking. Results in Table 2 indicate that random masking consistently outperforms others. While joint and temporal masking provide competitive results, group masking underperforms, suggesting that overly structured masking limits the model’s capacity to capture diverse patterns. Consequently, we adopt **random masking with 75% ratio** as our default strategy.

**More Skeleton Modalities.** In skeleton-based

	Image Pretrain	Skeleton Pretrain	MAE	DiffMAE
Linear-Probe	✓	✓	52.0	52.0
			72.2	71.3
	✓	✓	76.3	78.6
			81.4	<b>83.1</b>
Fine-tune	✓	✓	82.8	82.8
			86.8	86.5
	✓	✓	88.1	88.6
			90.5	<b>91.0</b>

TABLE 1: Ablation study of image pretrain, skeleton pretrain on NTU-60 C-sub.

Strategy	Ratio	Linear Probe	Fine-tune
Joint	75	82.3	90.4
Temporal	75	82.9	90.7
Random	75	<b>83.1</b>	<b>91.0</b>
Group	75	81.3	90.3

TABLE 2: Comparison of masking strategies on NTU-60 C-sub.

recognition, joint data can be further augmented by deriving motion and bone modalities. We evaluate these modalities individually and in combination using DiffMAE fine-tuning to assess their effectiveness within vision models. As shown in Table 3, joint features perform strongly, while motion and bone streams offer complementary cues. Fusing all three modalities significantly boosts performance, reaching 85.8% (linear probing) and 93.1% (fine-tuning). This confirms that this skeleton-modality fusion remains effective even when skeleton data is reformatted as images and processed by vision models. In subsequent main results, we report both the Joint stream (**S2I**) and the 3-stream fusion (**3s-S2I**).

#### 4.4 Comparison with the State-of-the-art Methods

**Linear Evaluation Results.** In linear evaluation, we freeze the pretrained backbone and train a supervised linear classifier on top. Table 4 summarizes results on NTU-60, NTU-120, and PKU-MMD. Despite using image-pretrained vision models without skeleton-specific architectures, our S2I achieves competitive performance

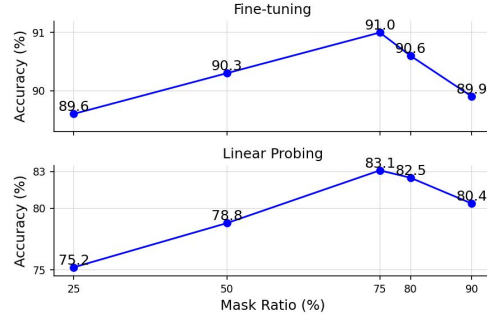


Fig. 3: Effect of mask ratio on NTU-60 C-sub.

Method	Linear Probe	Fine-tune
Joint	83.1	91.0
Motion	70.5	89.7
Bone	81.0	90.8
3-stream	<b>85.8</b>	<b>93.1</b>

TABLE 3: Comparison of skeleton modalities on NTU-60 C-sub.

compared to recent specialized methods. Specifically, S2I attains 83.1% and 88.0% on NTU-60 (C-sub and C-view), and 75.0% on NTU-120 (C-sub), demonstrating its effectiveness in bridging skeleton data with vision models. By integrating joint, motion, and bone streams, 3s-S2I further enhances representation quality, achieving state-of-the-art results on NTU-60 C-sub (85.8%), NTU-120 C-set (80.3%), and PKU II (62.0%).

**Fine-tuned Evaluation Results.** In a fine-tuned protocol, an MLP head is attached to the pretrained backbone, and the whole network is fully fine-tuned. As shown in Table 5, our S2I achieves competitive performance on NTU-60 and NTU-120 without introducing any skeleton-specific architectural designs. By bridging skeleton data with vision-pretrained models, S2I adapts effectively to skeleton tasks. With multi-stream fusion, 3s-S2I reaches state-of-the-art results, confirming the scalability of our approach.

**Semi-supervised Evaluation Results.** In the semi-supervised protocol, the post-attached classification layer and the pre-trained encoder are fine-tuned together with only a small fraction of the training set. We evaluate on NTU-60 with 1% and 10% labeled samples. As shown in Table 6,

Method	NTU-60		NTU-120		PKU-MMD	
	C-sub	C-view	C-sub	C-set	Phase I	Phase II
LongT GAN [49]	39.1	48.1	-	-	67.7	26.0
P&C [50]	50.7	76.3	42.7	41.7	59.9	25.5
MS <sup>2</sup> L [51]	52.6	-	-	-	64.9	27.6
SkeletonMAE [31]	74.8	77.7	72.5	73.5	82.8	36.1
3s-SkeletonCLR [26]	75.0	79.8	60.7	62.6	85.3	-
3s-Colorization [40]	75.2	83.1	-	-	-	-
ISC [52]	76.3	85.2	67.1	67.9	80.9	36.0
GL-Transformer [53]	76.3	83.8	66.0	68.7	-	-
3s-CrosSCLR [26]	77.8	83.4	67.9	66.7	84.9	21.2
3s-AimCLR [27]	78.9	83.8	68.2	68.8	87.4	39.5
CMD [54]	79.4	86.9	70.3	71.5	-	43.0
3s-CPM [28]	83.2	87.0	73.0	74.0	90.7	51.5
3s-ActCLR [55]	84.3	88.8	74.3	75.7	-	-
MAMP [29]	84.9	89.1	78.6	79.1	92.2	53.8
MacDiff [30]	<b>86.4</b>	<b>91.0</b>	<b>79.4</b>	<u>80.2</u>	<b>92.8</b>	-
S2I (Ours)	83.1	88.0	75.0	75.5	88.0	<u>57.4</u>
3s-S2I (Ours)	<u>85.8</u>	<u>89.7</u>	<u>78.9</u>	<b>80.3</b>	<u>92.3</u>	<b>62.0</b>

TABLE 4: Comparison of Linear Evaluation results on NTU 60, NTU and PKU datasets. 3s- represents the ensemble results of joint(J), bone(B) and motion(M) streams. **Bold** and underlined indicate the best and second best results, respectively. The same notation applies throughout.

Method	NTU-60		NTU-120	
	C-sub	C-view	C-sub	C-set
AimCLR (STFormer) [27]	83.9	90.4	74.6	77.2
CrosSCLR (STFormer) [26]	84.6	90.5	75.0	77.9
CPM [28]	84.8	91.1	78.4	78.9
3s-CrosSCLR [26]	86.2	92.5	80.5	80.4
3s-AimCLR [27]	86.9	92.8	80.1	80.9
SkeletonMAE [31]	86.6	92.9	76.8	79.1
3s-Colorization [40]	88.0	94.9	-	-
3s-ActCLR [55]	88.2	93.9	82.1	84.6
MCC [56]	89.7	96.3	81.3	83.5
ViA [57]	89.6	96.4	85.0	86.5
3s-Hi-TRS [58]	90.0	95.7	85.3	87.4
MAMP [29]	<b>93.1</b>	<u>97.5</u>	<u>90.0</u>	<b>91.3</b>
MacDiff [30]	92.7	97.3	-	-
S2I (Ours)	91.0	96.7	86.6	87.9
3s-S2I (Ours)	<b>93.1</b>	<b>97.7</b>	<b>90.2</b>	<u>91.2</u>

TABLE 5: Comparison of fine-tuned results on the NTU-60 and NTU-120 datasets.

our proposed S2I demonstrates strong performance with 71.4% (1%) and 88.4% (10%) under X-sub setting. With multi-stream fusion, 3s-S2I achieves state-of-the-art results, reaching 75.2% (1%) and 88.3% (10%), validating the effectiveness of S2I representation in low-label regimes.

**Transfer Learning Evaluation Results.** In the transfer learning protocol, models are pre-trained on a source dataset and then fine-tuned on a distinct target dataset, thereby assessing the gen-

Method	NTU-60			
	C-sub		C-view	
	(1%)	(10%)	(1%)	(10%)
LongT GAN [49]	35.2	62.0	-	-
MS <sup>2</sup> L [51]	33.1	65.1	-	-
ASSL [59]	-	64.3	-	69.8
ISC [52]	35.7	65.9	38.1	72.5
3s-CrosSCLR [26]	51.1	74.4	50.0	77.8
3s-Colorization [40]	48.3	71.7	52.5	78.9
CMD [54]	50.6	75.4	53.0	80.2
3s-Hi-TRS [58]	49.3	77.7	51.5	81.1
3s-AimCLR [27]	54.8	78.2	54.3	81.6
3s-CMD [54]	55.6	79.0	55.5	82.4
CPM [28]	56.7	73.0	57.5	77.1
SkeletonMAE [31]	54.4	80.6	54.6	83.5
MAMP [29]	66.0	88.0	68.7	91.5
MacDiff [30]	65.6	<u>88.2</u>	<u>77.3</u>	<b>92.5</b>
S2I (Ours)	<u>71.4</u>	84.8	73.3	87.8
3s-S2I (Ours)	<b>75.2</b>	<b>88.3</b>	77.7	<u>91.7</u>

TABLE 6: Comparison of semi-supervised results on the NTU-60 dataset.

eralization ability of the learned representations. In this setting, PKU-MMD II serves as the target dataset, while NTU-60, NTU-120, and PKU-MMD I are used as source datasets. As reported in Table 7, our proposed method achieves strong performance on PKU-MMD II across all transfer settings, demonstrating superior generalization and robustness compared to existing methods.

Method	To PKU-II		
	NTU-60	NTU-120	PKU-I
LongT GAN [49]	44.8	-	43.6
MS <sup>2</sup> L [51]	45.8	-	44.1
ISC [52]	51.1	52.3	45.1
CMD [54]	56.0	57.0	-
SkeletonMAE [31]	58.4	61.0	62.5
MAMP [29]	70.6	73.2	70.1
MacDiff [30]	<u>72.2</u>	<u>73.4</u>	<u>71.4</u>
S2I (ours)	70.2	71.6	68.1
3s-S2I (ours)	<b>72.6</b>	<b>73.9</b>	<b>72.9</b>

TABLE 7: Comparison of transfer learning results on PKUMMD II dataset.

Method	NTU120-Csub	NTU60-Csub	PKU-I-CS	PKU-II-CS	Toyota-CS	NW-UCLA
Self-pretrain	86.6	91.0	94.0	65.8	64.5	91.6
Universal-pretrain	<b>87.0</b>	<b>91.6</b>	<b>95.2</b>	<b>71.1</b>	<b>68.0</b>	<b>93.5</b>

TABLE 9: Universal pretraining evaluation on multiple skeleton datasets.

#### 4.5 Broader Applications

As discussed in Section 3.1, S2I provides a unified representation that supports both Cross-Format Transfer Learning and Universal Skeleton Representation Learning. To highlight its advantages, we conduct experiments under these two settings.

**Cross-Format Transfer Learning Evaluation Results.** We evaluate S2I on three heterogeneous skeleton datasets: NTU-60 (25 joints), Toyota (13 joints), and NW-UCLA (20 joints). Existing methods often rely on joint downsampling or interpolation to match skeleton formats, which can introduce information loss or noise. In contrast, our S2I preserves structural information by converting skeleton sequences into a format-agnostic image representation. As shown in Table 8, S2I achieves clear improvements over prior works. Notably, 3s-S2I reaches 53.8% on Toyota (CV1), surpassing existing methods by a significant margin. These results highlight the scalability and generalization ability of S2I for cross-format skeleton representation learning.

**Universal Representation Pretraining Evaluation Results.** To assess the generalizability of our representation, we perform universal representation learning by aggregating training data from multiple datasets (NTU120-Csub, PKU-I-

Method	NTU-60 (25 joints)		
	Toyota (13 joints) CS	CV1	NW-UCLA (20 joints)
Colorization [40]	-	-	<u>93.3</u>
UNIK [60]	63.1	22.9	-
ViA [57]	64.5	36.1	-
S2I (Ours)	<u>65.4</u>	<u>43.1</u>	93.2
3s-S2I (Ours)	<b>70.1</b>	<b>53.8</b>	<b>94.2</b>

TABLE 8: Cross-format transfer learning results from NTU-60 to Toyota and NW-UCLA datasets.

CS, PKU-II-CS, Toyota-CS, and NW-UCLA).<sup>2</sup> All experiments are conducted on joint data. As shown in Table 9, universal pretraining consistently boosts performance on all evaluated datasets compared to individual dataset self-pretraining. Notably, we obtain substantial gains on PKUV2-CS (+5.3%) and Toyota-CS (+3.5%), demonstrating the effectiveness of unified skeleton representation learning in leveraging diverse data sources to enhance generalization.

Collectively, the results from cross-format transfer learning (Table 8) and universal representation pretraining (Table 9) highlight the scalability and generalization of S2I, demonstrating its effectiveness as a unified representation.

## 5 CONCLUSION

In this paper, we propose Skeleton-to-Image Encoding (S2I), a simple yet effective representation that bridges spatio-temporal skeleton sequences with vision-pretrained models. By reformatting skeleton data into image-like structures, S2I enables the direct adoption of powerful pre-trained vision models without requiring skeleton-specific architectural modifications. Through extensive experiments on five benchmark datasets,

<sup>2</sup> More details of implementations and skeleton partitioning are provided in Appendix E.

we demonstrated that S2I achieves competitive performance for skeleton representation learning. Moreover, S2I naturally supports challenging evaluation scenarios, including cross-format transfer learning across heterogeneous skeleton layouts and universal skeleton pretraining by jointly leveraging diverse datasets, highlighting its scalability and generalization. In the future, we plan to extend S2I to other larger vision models (e.g., VLMs and multi-modal vision models) and explore its potential in multi-modal action recognition, including joint modeling with RGB videos and other sensor data.

## REFERENCES

- [1] A. Dosovitskiy, L. Beyer, A. Kolesnikov, D. Weissenborn, X. Zhai, T. Unterthiner, M. Dehghani, M. Minderer, G. Heigold, S. Gelly, J. Uszkoreit, and N. Houlsby, "An image is worth 16x16 words: Transformers for image recognition at scale," in *International Conference on Learning Representations*, 2021. [Online]. Available: <https://openreview.net/forum?id=YicbFdNTTy>
- [2] K. He, X. Chen, S. Xie, Y. Li, P. Dollár, and R. Girshick, "Masked autoencoders are scalable vision learners," in *Proceedings of the IEEE/CVF conference on computer vision and pattern recognition*, 2022, pp. 16 000–16 009.
- [3] C. Jia, Y. Yang, Y. Xia, Y.-T. Chen, Z. Parekh, H. Pham, Q. Le, Y.-H. Sung, Z. Li, and T. Duerig, "Scaling up visual and vision-language representation learning with noisy text supervision," in *Proceedings of the 38th International Conference on Machine Learning*, ser. Proceedings of Machine Learning Research, M. Meila and T. Zhang, Eds., vol. 139. PMLR, 18–24 Jul 2021, pp. 4904–4916. [Online]. Available: <https://proceedings.mlr.press/v139/jia21b.html>
- [4] A. Singh, R. Hu, V. Goswami, G. Couairon, W. Galuba, M. Rohrbach, and D. Kiela, "Flava: A foundational language and vision alignment model," in *Proceedings of the IEEE/CVF Conference on Computer Vision and Pattern Recognition*, June 2022, pp. 15 638–15 650.
- [5] Z. Xia and T. Wu, "Large language models can understand depth from monocular images," *arXiv preprint arXiv:2409.01133*, 2024.
- [6] L. Yang, B. Kang, Z. Huang, X. Xu, J. Feng, and H. Zhao, "Depth anything: Unleashing the power of large-scale unlabeled data," in *Proceedings of the IEEE/CVF Conference on Computer Vision and Pattern Recognition*, 2024, pp. 10 371–10 381.
- [7] T. Zhang, K. Ding, J. Wen, Y. Xiong, Z. Zhang, S. Xiang, and C. Pan, "Pad: Self-supervised pre-training with patchwise-scale adapter for infrared images," 2023.
- [8] J. N. Paranjape, C. de Melo, and V. M. Patel, "F-vita: Foundation model guided visible to thermal translation," *arXiv preprint arXiv:2504.02801*, 2025.
- [9] Z. Tong, Y. Song, J. Wang, and L. Wang, "VideoMAE: Masked autoencoders are data-efficient learners for self-supervised video pre-training," in *Advances in Neural Information Processing Systems*, 2022.
- [10] L. Wang, B. Huang, Z. Zhao, Z. Tong, Y. He, Y. Wang, Y. Wang, and Y. Qiao, "Videomae v2: Scaling video masked autoencoders with dual masking," in *Proceedings of the IEEE/CVF Conference on Computer Vision and Pattern Recognition*, June 2023, pp. 14 549–14 560.
- [11] J. Wang, D. Chen, Z. Wu, C. Luo, L. Zhou, Y. Zhao, Y. Xie, C. Liu, Y.-G. Jiang, and L. Yuan, "Omnivl: One foundation model for image-language and video-language tasks," *Advances in neural information processing systems*, vol. 35, pp. 5696–5710, 2022.
- [12] Z. Wang, X. Yu, Y. Rao, J. Zhou, and J. Lu, "P2p: Tuning pre-trained image models for point cloud analysis with point-to-pixel prompting," *Advances in neural information processing systems*, vol. 35, 2022.
- [13] R. Zhang, Z. Guo, W. Zhang, K. Li, X. Miao, B. Cui, Y. Qiao, P. Gao, and H. Li, "Pointclip: Point cloud understanding by clip," in *Proceedings of the IEEE/CVF conference on computer vision and pattern recognition*, 2022, pp. 8552–8562.
- [14] C. Wei, K. Mangalam, P.-Y. Huang, Y. Li, H. Fan, H. Xu, H. Wang, C. Xie, A. Yuille, and C. Feichtenhofer, "Diffusion models as masked autoencoders," in *Proceedings of the IEEE/CVF International Conference on Computer Vision*, 2023, pp. 16 284–16 294.
- [15] Y. Du, W. Wang, and L. Wang, "Hierarchical recurrent neural network for skeleton based action recognition," in *Proceedings of the IEEE conference on computer vision and pattern recognition*, 2015, pp. 1110–1118.
- [16] J. Liu, A. Shahroudy, D. Xu, A. C. Kot, and G. Wang, "Skeleton-based action recognition using spatio-temporal lstm network with trust gates," *IEEE transactions on pattern analysis and machine intelligence*, vol. 40, no. 12, pp. 3007–3021, 2017.
- [17] P. Zhang, C. Lan, J. Xing, W. Zeng, J. Xue, and N. Zheng, "View adaptive recurrent neural networks for high performance human action recognition from skeleton data," in *Proceedings of the IEEE International Conference on Computer Vision*, 2017, pp. 2117–2126.
- [18] Y. Du, Y. Fu, and L. Wang, "Skeleton based action recognition with convolutional neural network," in *2015 3rd IAPR Asian Conference on Pattern Recognition (ACPR)*. IEEE, 2015, pp. 579–583.
- [19] Q. Ke, M. Bennamoun, S. An, F. Sohel, and F. Bousaid, "A new representation of skeleton sequences for 3d action recognition," in *Proceedings of the IEEE conference on computer vision and pattern recognition*, 2017, pp. 3288–3297.
- [20] C. Li, Q. Zhong, D. Xie, and S. Pu, "Co-occurrence feature learning from skeleton data for action recognition and detection with hierarchical aggregation," in *Proceedings of the 27th International Joint Conference on Artificial Intelligence*, 2018, pp. 786–792.
- [21] S. Yan, Y. Xiong, and D. Lin, "Spatial temporal graph convolutional networks for skeleton-based action recognition," in *Thirty-Second AAAI conference on artificial intelligence*, 2018.

- [22] L. Shi, Y. Zhang, J. Cheng, and H. Lu, "Two-stream adaptive graph convolutional networks for skeleton-based action recognition," in *Proceedings of the IEEE/CVF Conference on Computer Vision and Pattern Recognition (CVPR)*, June 2019.
- [23] Y. Chen, Z. Zhang, C. Yuan, B. Li, Y. Deng, and W. Hu, "Channel-wise topology refinement graph convolution for skeleton-based action recognition," in *Proceedings of the IEEE/CVF International Conference on Computer Vision*, 2021, pp. 13 359–13 368.
- [24] Y. Zhang, B. Wu, W. Li, L. Duan, and C. Gan, "Stst: Spatial-temporal specialized transformer for skeleton-based action recognition," in *Proceedings of the 29th ACM International Conference on Multimedia*, 2021.
- [25] Y. Zhou, Z.-Q. Cheng, C. Li, Y. Fang, Y. Geng, X. Xie, and M. Keuper, "Hypergraph transformer for skeleton-based action recognition," *arXiv*, 2022.
- [26] L. Li, M. Wang, B. Ni, H. Wang, J. Yang, and W. Zhang, "3d human action representation learning via cross-view consistency pursuit," in *Proceedings of the IEEE/CVF conference on computer vision and pattern recognition*, 2021, pp. 4741–4750.
- [27] T. Guo, H. Liu, Z. Chen, M. Liu, T. Wang, and R. Ding, "Contrastive learning from extremely augmented skeleton sequences for self-supervised action recognition," in *Proceedings of the AAAI conference on artificial intelligence*, vol. 36, no. 1, 2022, pp. 762–770.
- [28] H. Zhang, Y. Hou, W. Zhang, and W. Li, "Contrastive positive mining for unsupervised 3d action representation learning," in *European Conference on Computer Vision*. Springer, 2022, pp. 36–51.
- [29] Y. Mao, J. Deng, W. Zhou, Y. Fang, W. Ouyang, and H. Li, "Masked motion predictors are strong 3d action representation learners," in *Proceedings of the IEEE/CVF International Conference on Computer Vision*, 2023, pp. 10 181–10 191.
- [30] L. Wu, L. Lin, J. Zhang, Y. Ma, and J. Liu, "Macdiff: Unified skeleton modeling with masked conditional diffusion," in *European Conference on Computer Vision*. Springer, 2024, pp. 110–128.
- [31] W. Wu, Y. Hua, C. Zheng, S. Wu, C. Chen, and A. Lu, "Skeletonmae: Spatial-temporal masked autoencoders for self-supervised skeleton action recognition," in *2023 IEEE international conference on multimedia and expo workshops*. IEEE, 2023, pp. 224–229.
- [32] K. He, H. Fan, Y. Wu, S. Xie, and R. Girshick, "Momentum contrast for unsupervised visual representation learning," in *Proceedings of the IEEE/CVF conference on computer vision and pattern recognition*, 2020.
- [33] T. Chen, S. Kornblith, M. Norouzi, and G. Hinton, "A simple framework for contrastive learning of visual representations," in *International conference on machine learning*. PmLR, 2020, pp. 1597–1607.
- [34] R. Qian, T. Meng, B. Gong, M.-H. Yang, H. Wang, S. Belongie, and Y. Cui, "Spatiotemporal contrastive video representation learning," in *Proceedings of the IEEE/CVF conference on computer vision and pattern recognition*, 2021, pp. 6964–6974.
- [35] H. Bao, L. Dong, S. Piao, and F. Wei, "BEit: BERT pre-training of image transformers," in *International Conference on Learning Representations*, 2022.
- [36] C. Wei, H. Fan, S. Xie, C.-Y. Wu, A. Yuille, and C. Feichtenhofer, "Masked feature prediction for self-supervised visual pre-training," in *Proceedings of the IEEE/CVF conference on computer vision and pattern recognition*, 2022, pp. 14 668–14 678.
- [37] M. Li, S. Chen, Y. Zhao, Y. Zhang, Y. Wang, and Q. Tian, "Dynamic multiscale graph neural networks for 3d skeleton based human motion prediction," in *Proceedings of the IEEE/CVF conference on computer vision and pattern recognition*, 2020, pp. 214–223.
- [38] Y. Cai, L. Ge, J. Liu, J. Cai, T.-J. Cham, J. Yuan, and N. M. Thalmann, "Exploiting spatial-temporal relationships for 3d pose estimation via graph convolutional networks," in *Proceedings of the IEEE/CVF international conference on computer vision*, 2019.
- [39] P. Zhang, C. Lan, W. Zeng, J. Xing, J. Xue, and N. Zheng, "Multi-scale semantics-guided neural networks for efficient skeleton-based human action recognition," *arXiv preprint arXiv:2111.03993*, 2021.
- [40] S. Yang, J. Liu, S. Lu, M. H. Er, and A. C. Kot, "Skeleton cloud colorization for unsupervised 3d action representation learning," in *Proceedings of the IEEE/CVF International Conference on Computer Vision*, 2021.
- [41] Q. Liu and Z. Wang, "Collaborating domain-shared and target-specific feature clustering for cross-domain 3d action recognition," in *European Conference on Computer Vision*. Springer, 2022, pp. 137–155.
- [42] A. Shahroudy, J. Liu, T.-T. Ng, and G. Wang, "Ntu rgb+d: A large scale dataset for 3d human activity analysis," in *Proceedings of the IEEE Conference on Computer Vision and Pattern Recognition*, June 2016.
- [43] J. Liu, A. Shahroudy, M. Perez, G. Wang, L. Y. Duan, and A. C. Kot, "Ntu rgb+d 120: A large-scale benchmark for 3d human activity understanding," *IEEE Transactions on Pattern Analysis and Machine Intelligence*, vol. 42, no. 10, pp. 2684–2701, 2020.
- [44] J. Liu, S. Song, C. Liu, Y. Li, and Y. Hu, "A benchmark dataset and comparison study for multi-modal human action analytics," *ACM Transactions on Multimedia Computing, Communications, and Applications (TOMM)*, vol. 16, no. 2, pp. 1–24, 2020.
- [45] J. Wang, X. Nie, Y. Xia, Y. Wu, and S.-C. Zhu, "Cross-view action modeling, learning and recognition," in *Proceedings of the IEEE Conference on Computer Vision and Pattern Recognition*, 2014, pp. 2649–2656.
- [46] S. Das, R. Dai, M. Koperski, L. Minciullo, L. Garattoni, F. Bremond, and G. Francesca, "Toyota smarhome: Real-world activities of daily living," in *The IEEE International Conference on Computer Vision*, 2019.
- [47] P. Zhang, C. Lan, W. Zeng, J. Xing, J. Xue, and N. Zheng, "Semantics-guided neural networks for efficient skeleton-based human action recognition," in *proceedings of the IEEE/CVF conference on computer vision and pattern recognition*, 2020, pp. 1112–1121.
- [48] K. Cheng, Y. Zhang, X. He, W. Chen, J. Cheng, and H. Lu, "Skeleton-based action recognition with shift graph convolutional network," in *Proceedings of the IEEE/CVF conference on computer vision and pattern recognition*, 2020, pp. 183–192.
- [49] N. Zheng, J. Wen, R. Liu, L. Long, J. Dai, and Z. Gong, "Unsupervised representation learning with

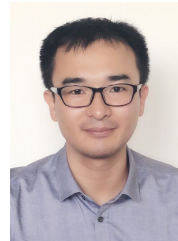
long-term dynamics for skeleton based action recognition," in *Proceedings of the AAAI conference on artificial intelligence*, vol. 32, no. 1, 2018.

- [50] K. Su, X. Liu, and E. Shlizerman, "Predict & cluster: Unsupervised skeleton based action recognition," in *Proceedings of the IEEE/CVF conference on computer vision and pattern recognition*, 2020, pp. 9631–9640.
- [51] L. Lin, S. Song, W. Yang, and J. Liu, "Ms2l: Multi-task self-supervised learning for skeleton based action recognition," in *Proceedings of the 28th ACM international conference on multimedia*, 2020, pp. 2490–2498.
- [52] F. M. Thoker, H. Doughty, and C. G. Snoek, "Skeleton-contrastive 3d action representation learning," in *Proceedings of the 29th ACM international conference on multimedia*, 2021, pp. 1655–1663.
- [53] B. Kim, H. J. Chang, J. Kim, and J. Y. Choi, "Global-local motion transformer for unsupervised skeleton-based action learning," in *European conference on computer vision*. Springer, 2022, pp. 209–225.
- [54] Y. Mao, W. Zhou, Z. Lu, J. Deng, and H. Li, "Cmd: Self-supervised 3d action representation learning with cross-modal mutual distillation," in *European Conference on Computer Vision*. Springer, 2022, pp. 734–752.
- [55] L. Lin, J. Zhang, and J. Liu, "Actionlet-dependent contrastive learning for unsupervised skeleton-based action recognition," in *Proceedings of the IEEE/CVF Conference on Computer Vision and Pattern Recognition*, 2023, pp. 2363–2372.
- [56] Y. Su, G. Lin, and Q. Wu, "Self-supervised 3d skeleton action representation learning with motion consistency and continuity," in *Proceedings of the IEEE/CVF international conference on computer vision*, 2021.
- [57] D. Yang, Y. Wang, A. Dantcheva, L. Garattoni, G. Francesca, and F. Brémond, "View-invariant skeleton action representation learning via motion retargeting," *International Journal of Computer Vision*, vol. 132, no. 7, pp. 2351–2366, 2024.
- [58] Y. Chen, L. Zhao, J. Yuan, Y. Tian, Z. Xia, S. Geng, L. Han, and D. N. Metaxas, "Hierarchically self-supervised transformer for human skeleton representation learning," in *European Conference on Computer Vision*. Springer, 2022, pp. 185–202.
- [59] C. Si, X. Nie, W. Wang, L. Wang, T. Tan, and J. Feng, "Adversarial self-supervised learning for semi-supervised 3d action recognition," in *European Conference on Computer Vision*, 2020, pp. 35–51.
- [60] D. Yang, Y. Wang, A. Dantcheva, L. Garattoni, G. Francesca, and F. Brémond, "Unik: A unified framework for real-world skeleton-based action recognition," *arXiv preprint arXiv:2107.08580*, 2021.
- [61] A. Vaswani, N. Shazeer, N. Parmar, J. Uszkoreit, L. Jones, A. N. Gomez, E. Kaiser, and I. Polosukhin, "Attention is all you need," *Advances in neural information processing systems*, vol. 30, 2017.
- [62] J. L. Ba, J. R. Kiros, and G. E. Hinton, "Layer normalization," *arXiv preprint arXiv:1607.06450*, 2016.
- [63] J. Ho, A. Jain, and P. Abbeel, "Denoising diffusion probabilistic models," *Advances in neural information processing systems*, vol. 33, pp. 6840–6851, 2020.
- [64] G. Rogez, P. Weinzaepfel, and C. Schmid, "Lcr-net++: Multi-person 2d and 3d pose detection in natural im-

ages," *IEEE transactions on pattern analysis and machine intelligence*, vol. 42, no. 5, pp. 1146–1161, 2019.



Siyuan Yang received the B.Eng. degree from Harbin Institute of Technology, China, the M.Sc. degree from Nanyang Technological University, Singapore, and the Ph.D. degree from the Interdisciplinary Graduate Programme at Nanyang Technological University, Singapore. He is currently a Wallenberg-NTU Presidential Postdoctoral Fellow at KTH Royal Institute of Technology. His research interests include computer vision, action recognition, and human pose estimation.



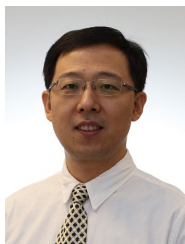
Jun Liu is a Professor and Chair in Digital Health at the School of Computing and Communications in Lancaster University. He got the PhD degree from Nanyang Technological University in 2019. He is an Associate Editor of IEEE TRANSACTIONS ON IMAGE PROCESSING, IEEE TRANSACTIONS ON INDUSTRIAL INFORMATICS, IEEE TRANSACTIONS ON BIOMETRICS, BEHAVIOR AND IDENTITY SCIENCE, *ACM Computing Surveys*, and *Pattern Recognition*. He has served as an Area Chair of CVPR, ECCV, ICML, NeurIPS, ICLR and MM.



Hao Cheng received the B.Eng. degree from the School of Software of Dalian University of Technology, China, in 2016, and the M.S. degree from the School of Computer Science and Technology, Tianjin University, China, in 2019. He received the Ph.D. degree in School of Electrical and Electronic Engineering from Nanyang Technological University, Singapore. He is currently an assistant professor with the School of Artificial Intelligence, Hebei University of Technology, China. His research interests include few-shot learning, class incremental learning, and computer vision.



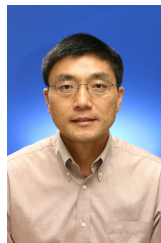
**Chong Wang** received the B.Eng. degree in Electronic Information Engineering from University of Electronic Science and Technology of China, China in 2019 and the M.S. degree in Signal Processing and Communications from University of Edinburgh, UK in 2020. He received the Ph.D. degree in School of Electrical and Electronic Engineering from Nanyang Technological University, Singapore in 2025. He is currently a Research Fellow in the School of Electrical and Electronic Engineering at Nanyang Technological University, Singapore. His research interests focus on image restoration and computational imaging.



**Dr. Shijian Lu** is an Associate Professor in the School of Computer Science and Engineering, Nanyang Technological University in Singapore. He obtained the PhD from the Electrical and Computer Engineering Department, National University of Singapore. Dr Shijian Lu's major research interests include image and video analytics, visual intelligence, and machine learning. He has published more than 100 international refereed journal and conference papers and co-authored over 10 patents in these research areas. He was also a top winner of the ICFHR2014 Competition on Word Recognition from Historical Documents, ICDAR 2013 Robust Reading Competition, etc. Dr Lu is an Associate Editor for the journal Pattern Recognition (PR) and Neurocomputing. He has also served in the program committee of several conferences, e.g., the Senior Program Committee of the International Joint Conferences on Artificial Intelligence (IJCAI) 2018 – 2021, etc.



**Hedvig Kjellstrom** is a Professor in the Department of Robotics, Perception and Learning at KTH Royal Institute of Technology, Sweden, and also affiliated with Swedish e-Science Research Centre and Max Planck Institute for Intelligent Systems, Germany. She received an MSc in Engineering Physics and a PhD in Computer Science from KTH in 1997 and 2001, respectively, and thereafter worked at the Swedish Defence Research Agency, before returning to a faculty position at KTH. Her present research focuses on methods for enabling artificial agents to interpret human and animal behavior. These ideas are applied in the study of human aesthetic bodily expressions such as in music and dance, modeling and interpreting human communicative behavior, and the understanding of animal behavior and experiences. In order to accomplish this, methods are developed for agents to perceive the world and build representations of it through vision. Hedvig has received several prizes for her research, including the 2010 Koenderink Prize for fundamental contributions in computer vision. She has written around 150 papers in the fields of computer vision, machine learning, robotics, information fusion, cognitive science, speech, and human-computer interaction. She is mostly active within computer vision, where she is an Editor-in-Chief for CVIU, a Program Chair for CVPR 2025, and regularly serves as Area Chair for the major conferences.



**Weisi Lin** is a President's Chair Professor in Computer Science, Nanyang Technological University, Singapore. His research interests include intelligent image processing, perceptual signal modeling, video compression, and multimedia communication. He is a Chartered Engineer and a fellow of IET. He serves as a General Co-Chair for IEEE ICME 2025 and Lead General Chair for IEEE ICIP 2027, and was a Technical Program Chair of the IEEE ICME 2013, PCM 2012, QoMEX 2014/2026 and IEEE VCIP 2017. He has been a Keynote/Invited/Panelist/Tutorial Speaker at over 50 international conferences, and was a Distinguished Lecturer of the IEEE Circuits and Systems Society from 2016 to 2017 and the Asia-Pacific Signal and Information Processing Association (APSIPA) from 2012 to 2013. He has been an Associate Editor of the IEEE Trans. Neural Networks and Learning Syst., the IEEE Trans. Image Process., the IEEE Trans. Circuits Syst. Video Technol., the IEEE Trans. Multimedia, and the IEEE Signal Process. Lett., as well as a Senior Editor for IEEE J. Selected Topics in Sig. Process. He has been awarded the Research Award 2023, College of Engineering, NTU, and is a Highly Cited Researcher since 2019 (awarded by Clarivate Analytics).



**Prof. Alex Kot** has been with the Nanyang Technological University, Singapore since 1991. He was Head of the Division of Information Engineering and Vice Dean Research at the School of Electrical and Electronic Engineering. Subsequently, he served as Associate Dean for College of Engineering for eight years. He is currently Professor and Director of Rapid-Rich Object

Search (ROSE) Lab and NTU-PKU Joint Research Institute. He has published extensively in the areas of signal processing, biometrics, image forensics and security, and computer vision and machine learning.

Dr. Kot served as Associate Editor for more than ten journals, mostly for IEEE transactions. He served the IEEE SP Society in various capacities such as the General Co-Chair for the 2004 IEEE International Conference on Image Processing and the Vice-President for the IEEE Signal Processing Society. He received the Best Teacher of the Year Award and is a co-author for several Best Paper Awards including ICPR, IEEE WIFS and IWDW, CVPR Precognition Workshop and VCIP. He was elected as the IEEE Distinguished Lecturer for the Signal Processing Society and the Circuits and Systems Society. He is a Fellow of IEEE, and a Fellow of Academy of Engineering, Singapore

**APPENDIX A  
NETWORK ARCHITECTURE AND CONFIGURATIONS**

**MAE [2].** Our MAE implementation follows the asymmetric encoder-decoder architecture proposed in [2]. The encoder is a Vision Transformer (ViT-B/16) [1], where “16” denotes the patch size. It operates only on the visible (unmasked) patches, without using any mask tokens. Each patch is linearly projected and added with fixed sinusoidal positional embeddings. The encoder consists of 12 Transformer blocks, each composed of a multi-head self-attention layer [61], a feed-forward MLP, and LayerNorm [62] applied before both submodules. A standard class token is used during fine-tuning but omitted during pretraining. The decoder is lightweight and receives both the encoded visible patches and learnable mask tokens. It comprises 8 Transformer blocks [61] with a hidden size of 512 and projects the output back to pixel space to reconstruct the original input. Reconstruction is performed only on masked patches, and the loss is computed as the mean squared error (MSE) between the predicted and ground-truth pixel values.

**DiffMAE [14].** Our implementation of DiffMAE follows the asymmetric encoder-decoder architecture proposed in [14], using ViT-B/16 as the encoder. The encoder processes only visible patches, and the decoder reconstructs masked regions from noisy inputs sampled through a forward diffusion process. Following the original design, we append a LayerNorm to the encoder output, followed by a linear projection to align feature dimensions with the decoder. Fixed sinusoidal positional embeddings are added to both the encoder and decoder inputs. We do not use relative positional encodings or layer scale. Additionally, separate linear projections are applied to clean and noisy tokens, respectively.

Unlike MAE, which directly regresses pixel values, DiffMAE formulates masked region prediction as a conditional generation task via a diffusion-based denoising process. Specifically, we adopt the *cross decoder* variant, where each noisy token (corresponding to a masked patch) independently attends to encoder outputs via

TABLE 10: Pretraining settings for MAE on S2I representation.

Config	Value
Optimizer	AdamW
Base learning rate	1.5e-4
Weight decay	0.05
Optimizer momentum	$\beta_1, \beta_2 = 0.9, 0.95$
Batch size	512
Learning rate schedule	cosine decay
Epochs	800
Warmup epochs	40
Augmentation	Horizontal flip (p=0.5), Random rotation, Random affine, Gaussian noise

cross-attention, without interacting with other noise tokens. This avoids shortcut paths and promotes more effective encoder pretraining. For the diffusion process, we follow a linear variance schedule [63], with the number of timesteps set to  $T = 1000$ .

**APPENDIX B  
PRETRAINING SETUP AND STRATEGIES**

**MAE [2].** We follow the general pretraining setup of MAE [2], with modifications to accommodate the smaller scale and different nature of skeleton datasets compared to ImageNet. Specifically, we use a batch size of 512 and train for 800 epochs. For data augmentation, we employ a customized pipeline designed for S2I skeleton representation. In contrast to the original MAE, which uses standard image augmentations such as ColorJitter and DropPath, we adopt lightweight and semantically consistent transformations: random horizontal flip ( $p = 0.5$ ), random rotation, random affine scaling and translation, and additive Gaussian noise with standard deviation. All augmentations are applied before normalization. All other components, including optimizer settings and learning rate schedule, remain consistent with the original MAE. The full configuration is summarized in Table 10.

**DiffMAE [14].** We follow the official DiffMAE pretraining setup on ImageNet, using the same optimizer, learning rate schedule, and number of training epochs (1600). To account for the smaller scale of skeleton dataset, we reduce the batch size to 512. In place of RandomResizedCrop, we adopt a skeleton-related augmentation pipeline

TABLE 11: Pretraining settings for DiffMAE on S2I representation.

Config	Value
Optimizer	AdamW
Weight decay	0.05
Base learning rate	1.5e-4
Optimizer momentum	$\beta_1, \beta_2 = 0.9, 0.95$
Batch size	512
Learning rate schedule	cosine decay
Epochs	1600
Warmup epochs	40
Augmentation	Horizontal flip (p=0.5), Random rotation, Random affine, Gaussian noise

consisting of horizontal flip, random rotation, affine transformation, and additive Gaussian noise, as detailed above. The full pretraining configuration is summarized in Table 11.

For the diffusion process, we follow the noise schedule formulation in [14], where each forward sample  $x_t^m$  is reparameterized as:

$$x_t^m = \sqrt{\alpha_t}x_0^m + \sqrt{1 - \alpha_t}\epsilon,$$

with  $\alpha_t = 1 - \beta_t$  and  $\bar{\alpha}_t = \prod_{i=1}^t \alpha_i$ . To control the noise level, we introduce a hyperparameter  $\rho$  following [14], which modulates the variance schedule by exponentiating each  $\beta_t$  as  $\beta_t^\rho$ . We set  $\rho = 1.0$  by default, which recovers the standard linear schedule in [63], where  $\beta_t$  increases linearly from  $10^{-4}$  to 0.02.

### APPENDIX C DOWNSTREAM TRAINING PROTOCOLS: FINE-TUNING AND LINEAR PROBING

We extract features from the encoder output for downstream tasks, including fine-tuning and linear probing. Following the standard ViT design [1], which includes a class token, we append an auxiliary dummy token to the input sequence during pretraining, as in [2]. This token is treated as the class token and used for classification in both fine-tuning and linear probing.

**Fine-tuning.** Our fine-tuning protocol follows standard supervised ViT training [1], with simplified configurations tailored for skeleton-based inputs. Specifically, we omit image-based data augmentation and regularization techniques such as RandAugment, label smoothing, mixup, and

TABLE 12: Fine-tuning settings for S2I representation.

Config	Value
Optimizer	AdamW
Base learning rate	1e-3
Weight decay	0.05
Layer-wise lr decay	0.75
Batch size	128 (NTU/PKU/Toyota), 32 (N-UCLA)
Learning rate schedule	cosine decay
Warmup epochs	10
Training epochs	100
Augmentation	Horizontal flip (p=0.5), Random rotation, Random affine, Gaussian noise

TABLE 13: Linear probing settings for S2I representation.

Config	Value
Optimizer	SGD
Base learning rate	2e-1
Weight decay	0
optimizer momentum	0.9
Batch size	128
Learning rate schedule	cosine decay
Warmup epochs	10
Training epochs	100
Augmentation	Horizontal flip (p=0.5), Random rotation, Random affine, Gaussian noise

cutmix. Instead, we apply a skeleton-related augmentation pipeline, including horizontal flip, rotation, affine transformation, and Gaussian noise. We use the AdamW optimizer with a base learning rate of  $1e-3$  and a cosine learning rate decay schedule. Layer-wise learning rate decay is applied with a decay rate of 0.75, following [35]. We set the batch size to 128 for NTU-60, NTU-120, PKU-MMD, and Toyota datasets, and reduce it to 32 for the smaller NW-UCLA dataset to prevent overfitting. The warmup period is fixed to 10 epochs, and training is performed for 100 epochs in total.

**Linear probing.** For linear probing, we freeze the encoder and train only a linear classification head on top of the extracted features. We follow a simplified setup without additional regularization such as weight decay, label smoothing, or mixup. The optimizer is SGD with a base learning rate of 0.2, cosine decay schedule, and momentum set to 0.9. A warmup of 10 epochs is applied, and training is conducted for 100 epochs in total. We use the same skeleton-related data augmentation as in fine-tuning. Detailed configurations are listed in Table 13.

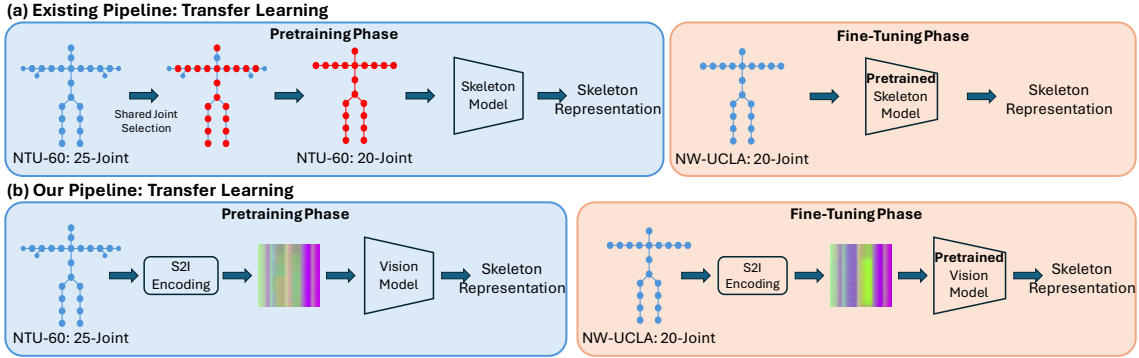


Fig. 4: Comparison between the existing skeleton-specific pipeline and our proposed S2I-based pipeline for transfer learning across datasets. (a) Existing methods first align joint formats before pretraining and fine-tuning on target datasets, which may lead to information loss. (b) Our approach bypasses manual joint selection by encoding the raw skeleton sequence into an image via S2I, enabling unified processing across datasets using a vision model.

**APPENDIX D  
 PIPELINE COMPARISON UNDER CROSS-FORMAT AND UNIVERSAL SETTINGS**

**Cross-Format Representation Learning.** To evaluate cross-format transfer performance, we compare our pipeline against the conventional transfer learning paradigm, using the transfer from NTU-60 to NW-UCLA as an example. As illustrated in Figure 4, existing approaches typically begin by manually downsampling the NTU-60 skeleton data (25 joints) to a shared 20-joint subset. A model is then pretrained on this reduced-format data and fine-tuned on NW-UCLA, which naturally adopts the 20-joint format. This process requires explicit joint alignment and may introduce structural mismatches, potentially degrading the quality of learned representations.

In contrast, our S2I-based pipeline removes the need for manual joint selection. We directly encode the raw skeleton sequences—regardless of their joint format—into semantically structured image-like representations. Both NTU-60 and NW-UCLA inputs are processed uniformly by the same visual backbone without any format-specific adaptation. This design enables seamless cross-format transfer while preserving the structural integrity of the original data. Figure 4 provides a visual comparison of the two pipelines,

highlighting the simplicity and universality of our approach for cross-format transfer learning.

**Universal Representation Pretraining.** To facilitate universal skeleton representation learning across diverse datasets, we compare our unified pipeline with traditional skeleton-specific approaches. As shown in Figure 5, conventional methods require designing and training separate models tailored to each joint format (e.g., 25-joint, 20-joint, 13-joint), resulting in limited scalability.

In contrast, our approach leverages the S2I (Skeleton-to-Image) encoding to transform skeleton sequences with arbitrary joint formats into structured image representations. These representations are then processed by a shared backbone model, enabling consistent and format-agnostic feature learning. This unified design eliminates the need for joint-level alignment or model reconfiguration, allowing all skeleton datasets—regardless of their original format—to contribute to a single pretraining framework. The resulting representation is thus inherently universal, capable of generalizing across different skeleton domains with no structural compromises.

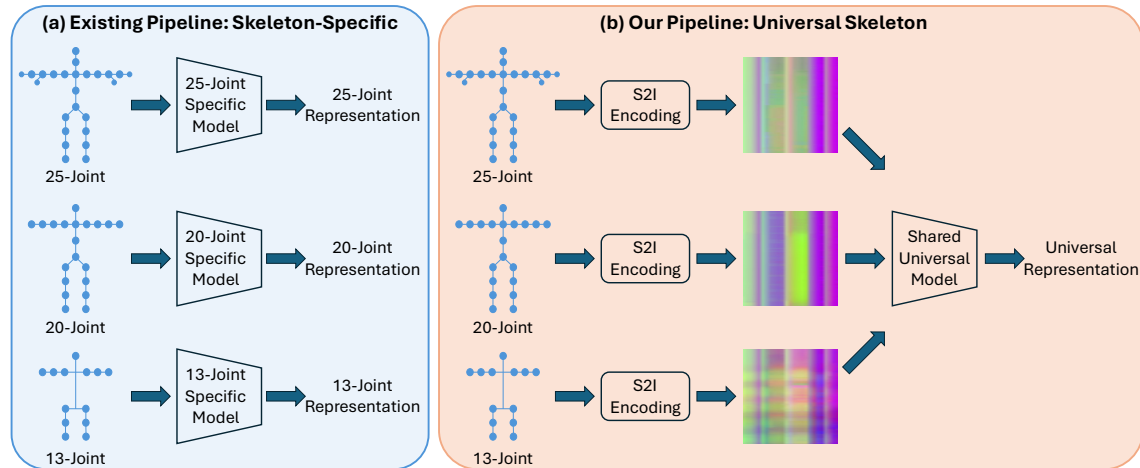


Fig. 5: Comparison of skeleton-specific and universal representation learning pipelines. (a) Conventional methods require format-specific models for each skeleton format. (b) Our method encodes arbitrary skeleton formats into image representations via S2I, enabling unified pretraining with a single backbone model.

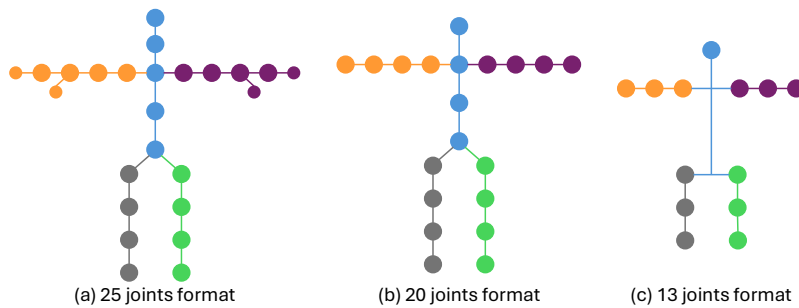


Fig. 6: Visualization of three commonly used skeleton formats: (a) 25-joint (NTU/PKU), (b) 20-joint (NW-UCLA), and (c) 13-joint (Toyota). Each skeleton is partitioned into five semantic body parts—Spine, Left Arm, Right Arm, Left Leg, and Right Leg—highlighted in different colors to ensure consistent representation across formats.

## APPENDIX E UNIVERSAL REPRESENTATION PRETRAINING SETUPS

**Implementation Details.** To conduct the Universal Representation Pretraining experiments, we utilize the training splits from multiple datasets, including NTU120 (C-sub) [43], PKU-MMD I (CS) [44], PKU-MMD II (CS), Toyota-Smarthome (CS) [46], and NW-UCLA [45]. Since the NTU60-

C-sub [42] training set is a subset of NTU120-C-sub, it is not explicitly included.

To ensure consistent input distribution across datasets, we compute the mean and standard deviation of the S2I RGB representations from the NTU120 C-sub training split, and use them to normalize the S2I inputs from all other datasets for scale alignment and stable optimization. Additionally, due to the increased size of the combined training data, we increase the batch size

TABLE 14: Semantic body part partitioning across different skeleton formats, using joint names.

Body Part	NTU/PKU (25 joints)	NW-UCLA (20 joints)	Toyota (13 joints)
Spine	head, neck, spine, middle of spine, base of spine	head, spine, middle of spine, base of spine	head
Left Arm	left shoulder, left elbow, left wrist, left hand, left thumb, tip of left hand	left shoulder, left elbow, left wrist, left hand	left shoulder, left elbow, left wrist
Right Arm	right shoulder, right elbow, right wrist, right hand, right thumb, tip of right hand	right shoulder, right elbow, right wrist, right hand	right shoulder, right elbow, right wrist
Left Leg	left hip, left knee, left ankle, left foot	left hip, left knee, left ankle, left foot	left hip, left knee, left ankle
Right Leg	right hip, right knee, right ankle, right foot	right hip, right knee, right ankle, right foot	right hip, right knee, right ankle

from 512 to 768, while keeping all other training configurations unchanged. All datasets are jointly trained in a unified manner, rather than using any sequential or curriculum-based strategy.

**Skeleton Partitioning for Different Formats.** To support universal skeleton representation learning across datasets with different joint formats, we consider three commonly used skeleton configurations, as shown in Figure 6. The NTU-60, NTU-120, and PKU-MMD datasets adopt the 25-joint layout extracted by Kinect V2. NW-UCLA provides 20-joint skeletons from Kinect V1, while the Toyota dataset offers 13-joint skeletons estimated using LCRNet [64].

To enable format-invariant learning, we partition the skeleton into five consistent body parts: *Spine*, *Left Arm*, *Right Arm*, *Left Leg*, and *Right Leg*. Figure 6 color-codes these body parts across the three skeleton formats, and Table 14 lists the corresponding joint names for each part.